

# UCLA

## UCLA Previously Published Works

### Title

High-resolution metabolic mapping of the cerebellum using 2D zoom magnetic resonance spectroscopic imaging

### Permalink

<https://escholarship.org/uc/item/4996z82k>

### Journal

Magnetic Resonance in Medicine, 85(5)

### ISSN

0740-3194

### Authors

Emir, Uzay E  
Sood, Jaiyta  
Chiew, Mark  
[et al.](#)

### Publication Date

2021-05-01

### DOI

10.1002/mrm.28614

Peer reviewed



Published in final edited form as:

*Magn Reson Med.* 2021 May ; 85(5): 2349–2358. doi:10.1002/mrm.28614.

## High-resolution metabolic mapping of the cerebellum using 2D zoom magnetic resonance spectroscopic imaging

Uzay E. Emir<sup>1,2</sup>, Jaiyta Sood<sup>1</sup>, Mark Chiew<sup>3</sup>, Micheal Albert Thomas<sup>4</sup>, Sean P. Lane<sup>5</sup>

<sup>1</sup>School of Health Sciences, Purdue University, West Lafayette, Indiana, USA

<sup>2</sup>Weldon School of Biomedical Engineering, Purdue University, West Lafayette, Indiana, USA

<sup>3</sup>Wellcome Centre for Integrative Neuroimaging, University of Oxford, Oxford, United Kingdom

<sup>4</sup>Department of Radiology, University of California Los Angeles, Los Angeles, California, USA

<sup>5</sup>Department of Psychological Sciences, Purdue University, West Lafayette, Indiana, USA

### Abstract

**Purpose:** The human cerebellum plays an important role in the functional activity of the cerebrum, ranging from motor to cognitive systems given its relaying role between the spinal cord and cerebrum. The cerebellum poses many challenges to Magnetic Resonance Spectroscopic Imaging (MRSI) due to its caudal location, susceptibility to physiological artifacts, and partial volume artifacts resulting from its complex anatomical structure. Thus, in the present study, we propose a high-resolution MRSI acquisition scheme for the cerebellum.

**Methods:** A zoom or reduced field of view (rFOV) metabolite-cycled MRSI acquisition at 3 Tesla, with a grid of  $48 \times 48$ , was developed to achieve a nominal resolution of  $62.5 \mu\text{L}$ . Single-slice rFOV MRSI data were acquired from the cerebellum of 5 healthy subjects with a nominal resolution of  $2.5 \times 2.5 \times 10 \text{ mm}^3$  in 9.6 min. Spectra were quantified using the LCMoDel package. A spatially unbiased atlas template of the cerebellum was used to analyze metabolite distributions in the cerebellum.

**Results:** The superior quality of the achieved spectra-enabled generation of high-resolution metabolic maps of total N-acetylaspartate, total Creatine (tCr), total Choline (tCho), glutamate+glutamine, and myo-inositol, with Cramér-Rao lower bounds below 50%. A template-based regions of interest (ROI) analysis resulted in spatially dependent metabolite distributions in 9 ROIs. The group-averaged high-resolution metabolite maps across subjects increased the contrast-to-noise ratio between cerebellum regions.

**Conclusion:** These findings indicate that very high-resolution metabolite probing of the cerebellum is feasible using rFOV or zoomed MRSI at 3 Tesla.

---

**Correspondence:** Uzay Emir, School of Health Sciences, Purdue University, School of Health Sciences, 550 Stadium Mall Drive, West Lafayette, IN 47907, USA. [uemir@purdue.edu](mailto:uemir@purdue.edu), **TWITTER**, [Uzay E. Emir @uzemye](https://twitter.com/uzemye).

SUPPORTING INFORMATION

Additional Supporting Information may be found online in the Supporting Information section.

## Keywords

cerebellum; concentric rings; metabolic map; reduced field of view; spectroscopic imaging

---

## 1 | INTRODUCTION

Compared to the cerebrum, the cerebellum constitutes only 10% of total brain volume; however, it has 3 times more neurons than the cerebrum<sup>1</sup> and consumes around 20% of the whole energy utilization of the brain.<sup>2</sup> The human cerebellum plays an important role in functional activity of the brain, which ranges from motor to cognitive systems due to its relaying role between the spinal cord and cerebrum. With the development of neuroimaging modalities, the cerebellum has been a focus of interest, but its complex structure and caudal location pose technical challenges for imaging modalities.<sup>3</sup> Increasingly, advanced MRI technologies, including anatomical and functional modalities, have facilitated the evaluation of the cerebellum.<sup>4,5</sup> This is of great importance because abnormalities in the cerebellum are associated with many neurological, neurodevelopmental, and psychiatric disorders.<sup>6-9</sup>

Magnetic Resonance Spectroscopy (MRS) techniques are increasingly used to enable the neurochemical probing of brain tissue.<sup>10</sup> Single voxel (SV) MRS has been the method of choice to study the cerebellum, with a nominal voxel dimension ranging from 4090  $\mu\text{L}$ <sup>11</sup> to 15620  $\mu\text{L}$ <sup>12</sup> for different neurological conditions. However, spectra in single SV-MRS acquisitions are derived from a mixture of different tissue compartments, which results in a partial volume effect. This partial volume effect is particularly problematic in the cerebellum due to its complex structures.

Alternatively, MRS imaging (MRSI) methods record multiple spectra from different regions simultaneously. The widespread use of MRSI has been limited by several challenges, including low signal to noise ratio (SNR) due to suboptimal sequences, inhomogeneity of the main ( $B_0$ ) and radiofrequency ( $B_1$ ) magnetic fields, and long acquisition times.<sup>13</sup> As increasingly advanced MRI acquisition and reconstruction approaches have been developed, sensitivity and resolution of MRSI have drastically improved. Recently, a nominal resolution of 110  $\mu\text{L}$  has been reported for 3D-MRSI of the whole-cerebrum at 3 Tesla (T).<sup>14</sup> Further improvements in resolution up to 36  $\mu\text{L}$  have been reported with the use of constrained reconstruction of 3D-MRSI at 3T.<sup>15</sup> Simultaneously, efforts at ultrahigh field (UHF 7T) MRI have resulted in further improvements in resolution both for 2D and 3D MRSI. A nominal resolution of 24  $\mu\text{L}$  with an acquisition duration of 46 min has been reported at 9.4T using 2D MRSI.<sup>16</sup> As for the 3D-MRSI, a nominal resolution of 20  $\mu\text{L}$  has been achieved within 17 min at 7T.<sup>17</sup> Although there have been numerous achievements for neurochemical mapping cerebrum using MRSI both at 3T and UHF, the cerebellum has not been a focus of interest due to the caudal location and the susceptibility to physiological artefacts. Only very few studies have been performed using MRSI in the cerebellum, with coarse nominal resolutions ranging from 310  $\mu\text{L}$ <sup>18</sup> to 1210  $\mu\text{L}$ .<sup>19</sup>

Zoom-MRI or reduced field of view (rFOV) acquisition schemes overcome the limitations of spatial resolution and low SNR for MRI. This has been achieved using outer volume suppression<sup>20</sup> or a well-defined spatial excitation.<sup>21</sup> Similar to zoom-MRI, 3-pulse

localization of MRSI suppresses the signal outside of the FOV and is used for rFOV MRSI measurements to reduce acquisition duration by reducing the number of phase-encoding steps.<sup>22,23</sup> In contrast to previous rFOV MRSI implementations, the present study sought to develop an accelerated rFOV acquisition scheme without reducing phase encoding steps for high-resolution short TE semi-LASER MRSI at 3T with a nominal resolution of 62.5  $\mu\text{L}$ . In order to increase the SNR of the zoomed acquisition, k-space data were acquired with a sampling density proportional to a Hanning window.<sup>24</sup> Further SNR gain was achieved using a narrower acquisition bandwidth. In 5 healthy subjects, we demonstrated that the proposed rFOV-MRSI with accelerated k-space trajectory generates high-resolution metabolic maps at 3T across an entire cerebellum slice with a thickness of 10 mm. Finally, we explored neurochemical alterations in regions of interest (ROIs) of the cerebellum using the spatially unbiased atlas template of the cerebellum (SUIT atlas).<sup>4</sup>

## 2 | METHODS

Five healthy subjects (3 females,  $25.5 \pm 7.07$  years [mean  $\pm$  standard deviation (SD)]) participated. All subjects provided informed consent before the in vivo MRI exam, which was approved by the Purdue University Institutional Review Board. Before being scanned, informed written assent was obtained from all the subjects.

### 2.1 | MRI data acquisition

The data were acquired using a Siemens Prisma 3T MR system (Siemens, Germany) with a 64-channel ( $N_{\text{channels}}$ ) head array receive coil. A T1-weighted MPRAGE dataset (TR = 1900 ms, TE = 2.13 ms, TI = 900 ms, flip angle =  $8^\circ$ , 176 transverse slices,  $0.9 \times 0.9 \times 1 \text{ mm}^3$  voxels) was acquired for each subject for MRSI acquisition planning.  $B_0$  shimming was achieved using the vendor-provided procedure, gradient echo shimming. The vendor-provided “patient-specific”  $B_1$  shimming option was used.

### 2.2 | Reduced FOV or zoom metabolite-cycled semi-laser MRSI

Metabolite-cycling MRSI was acquired using the same parameters as described in Emir et al.<sup>25</sup> Briefly, before the semi-LASER localization, 2 asymmetric inversion RF pulses in alternating TRs were used for downfield/upfield ( $N_{\text{directions}} = 2$  [upfield/downfield]) measurements.

The semi-LASER localization (Figure 1A) (Supporting Information Figure S1) was positioned in the central cerebellar slice in the transverse plane, without any angulation, to include right crus I, left crus I, and dentate nuclei (Figure 1B). The high in-plane nominal resolution ( $2.5 \text{ mm} \times 2.5 \text{ mm}$ ) with a thickness 10 mm was achieved using rFOV =  $120 \text{ mm} \times 120 \text{ mm} \times 10 \text{ mm}$ , semi-LASER localization =  $100\text{-}90 \text{ mm} \times 50\text{-}40 \text{ mm} \times 10 \text{ mm}$ , TR = 1500 ms, and TE = 32 ms. The semi-LASER volume of interest was placed asymmetrical in the rFOV.

To cover the  $48 \times 48$  grid in a rFOV, we modified our 2D-density weighted concentric ring trajectory (DW-CRT) design.<sup>24</sup> Each ring in DW-CRT consisting of 64 points (number of points per ring,  $N_{\text{p\_ring}} = 64$ ) was collected with an analog-digital-converter bandwidth of 40 kHz. This resulted in 128 spectral points ( $N_{\text{sp}} = 128$ ). Two temporal interleaves

(number of temporal interleaves,  $N_{ti} = 2$ ) with inverted readout gradients were collected with an spectral bandwidth of 625 Hz.<sup>24</sup> The total acquisition window was 205 ms for 256 spectral points. The rest of the DW-CRT parameters were identical to the previous 3T and 7T implementations<sup>24,26</sup>: 4 spatial interleaves ( $N_{si} = 4$  and  $N_{avg} = 1$ ) of 24 DW concentric rings ( $N_{ring} = 24$ ) were acquired with  $\alpha = 1$ . The total duration for the DW-CRT was 9 min 36 s ( $(N_{si} = 4) \times (N_{directions} = 2) \times (N_{ring} = 24) \times (N_{ti} = 2) \times (TR = 1500 \text{ ms}) = 576 \text{ s}$ ).

### 2.3 | Postprocessing

MatLab (R2016b, MathWorks, Natick, MA) was used for reconstruction. To achieve the full spectral bandwidth (1250 Hz), non-uniform fourier transform<sup>27</sup> was used to calculate the Fourier transform of the acquired k-space data.<sup>24</sup> The metabolite-cycled spectra were processed as described in Emir et al.<sup>25</sup> A Gaussian filter of 250-ms timing parameters was applied to the FIDs. The non-water-suppressed spectra-enabled frequency and phase corrections for each voxel with a dimension of 62.5  $\mu\text{L}$ . The metabolite spectra were obtained via subtracting the upfield and downfield FIDs, whereas summing them generated the water-only spectra. The remaining water signal in the metabolite spectrum was removed using the Hankel-Lanczos singular value decomposition.<sup>28</sup> A lipid-basis penalty algorithm was used to minimize the lipid contamination.<sup>29</sup> Water-only and metabolite-only whole cerebellum slice images were used to generate a brain and lipid mask for the lipid-basis penalty algorithm.

### 2.4 | Metabolite quantification

Metabolite quantification was performed using LCModel package (Version 6.3-1M).<sup>30</sup> The model spectra including 8 LCModel-simulated macromolecule resonances (positioned at 0.91, 1.21, 1.43, 1.67, 1.95, 2.08, 2.25, and 3 ppm) was used as a basis set for the LCModel analysis, as described in Steel et al.<sup>26</sup> The basis set included the model spectra of alanine, aspartate, ascorbate/vitamin C, glycerophosphocholine, phosphocholine (PCho), creatine (Cr), phosphocreatine (PCr), GABA, glucose, glutamine (Gln), glutamate (Glu), glutathione, lactate, myo-inositol (myo-ins), N-acetyl-aspartate (NAA), N-acetylaspartylglutamate (NAAG), phosphoethanolamine, scyllo-Inositol, and taurine. The LCModel fitting was performed over the spectral range from 0.5 to 4.2 ppm. The resulting Cramér-Rao lower bounds of estimated metabolites less than 50% were reported. Summed metabolite estimations were reported for total NAA (NAA+NAAG, tNAA), total Cr (Cr + PCr, tCr), total Cho (GPC + PCho, tCho), and Glu and Gln (Glu + Gln, Glx) because their pairwise-correlation estimates were high (correlation coefficient  $< -0.5$ ). The normalized metabolite levels were reported for each subject using the water-scaled signal intensity of each metabolite (raw):

$$\text{Metabolite - normalized} = \text{Metabolite - raw} / (\text{tCho}_{\text{raw}} + \text{tCr}_{\text{raw}} + \text{tNAA}_{\text{raw}} + \text{myo - Ins}_{\text{raw}} + \text{Glx}_{\text{raw}}).$$

Metabolite levels were also reported using water scaling and relative to tCr approaches. These metabolite levels were not corrected for  $T_1$  and  $T_2$  effects, partial volume, and water content differences.

## 2.5 | Regional distributions of neurochemical in the cerebellum

The cerebellar ROIs were obtained using the Cerebellar MNI FNIRT Maxprob thr25-2 mm of SUI Atlas (<http://www.diedrichsenlab.org/imaging/propatlas.htm>). Each subject's MRSI slice and metabolite maps was determined in the MPRAGE image space using statistical parametric mapping.<sup>31</sup> The resulting MRSI resolution was  $0.9 \times 0.9 \times 1 \text{ mm}^3$ . Then, ROIs of the SUI atlas were warped into each subject's MPRAGE image space in the following manner (Supporting Information Figure S2): each subject's MPRAGE image was nonlinearly registered to the Montreal Neurological Institute-152 template using the FMRIB nonlinear registration tool (FNIRT); afterward, the resulting warp field was applied to the Cerebellar MNI FNIRT Maxprob thr25-2 mm of the SUI atlas to transform them to each subject's MPRAGE image. Mean metabolite levels in cerebellar ROIs were calculated using *fslstats*<sup>32</sup> in the center slice of MRSI in the transverse plane.

To generate group-averaged metabolite spatial maps, metabolite maps were transformed to the MNI-152 template by applying the resulting warp field; afterward, metabolite maps were averaged across the 5 subjects.

## 2.6 | Statistical analysis

Only the ROIs that were consistently detected across subjects (in at least half of the subjects) were included in statistical analyses. As a secondary filter to select reliable ROIs, the mean number of voxels in each ROIs had to be 1 SD above the mean SD.

The mean regional metabolite-normalized levels from the aforementioned reliable ROIs of cerebellar atlas were used for statistical analyses using SAS software v.9.4 (SAS Institute, Cary, NC). MRS data from different ROIs were compared using a 1-way repeated measures analysis of variance separately for each reported normalized metabolites (tNAA, tCr, tCho, Glx, and myo-ins) across each target brain region (within-subject factor). Given the occurrence of missing data due to exclusion for unreliability, we utilized restricted maximum likelihood to fit the models. Each analysis examined the differences in MRS data across 9 ROIs, resulting in 36 possible pairwise comparisons. We employed a Benjamini-Hochberg correction within each family of comparisons in order to control the false discovery rate.<sup>33</sup> The same statistical analysis was performed for the water-scaled and relative to tCr approaches.

## 3 | RESULTS

Figure 1A shows coronal, sagittal, and axial images of an anatomical scan, including the placement of the MRSI slice and semi-LASER localization. The image derived from the non-water suppressed MRSI data shows the signals from the cerebellum. ROIs of the SUI atlas encompassed by the MRSI localization are illustrated in Figure 1B. The list of ROIs and the mean number of voxels for each metabolite that met our criteria for reliable quantification in the SUI atlas are listed in Table 1.

Figure 2A,B show the zoomed MRSI spectra with LCModel fits. Even at a nominal resolution of  $62.5 \mu\text{L}$  at 3T, spectra from 5 different volumes of interest are of high quality enough for reliable quantitation. Although LCModel-simulated macromolecule resonances

account for most of residual lipid signal in the spectral range of 0.5 to 1.8 ppm, some voxels have negative peaks at 1.8 ppm (gray box in Figure 2B) due to regularization error of the L2 lipid removal procedure.

The mean CRLB values for each ROI across subjects are reported in Table 2. In most of the voxels, the mean CRLB values after the Gaussian filter resulted in values less than 30% for the metabolites tNAA, tCr, tCho, myo-ins, and Glx. The resulting normalized metabolite maps and corresponding CRLB maps of a healthy subject are illustrated in Figure 3A,B, respectively.

Figure 4 shows the group-average metabolite maps of normalized metabolite levels in the MNI-152 template space. The mean normalized metabolite levels that met our criteria for reliable quantification in cerebellar ROIs (9 cerebellar ROIs) of the SUIT atlas are shown in Figure 5 (Supporting Information Table S1). The normalized metabolite levels revealed different neurochemical profiles that may characterize different cerebellar regions (Supporting Information Table S4). For instance, the tCho, tNAA, and myo-ins levels in the dentate nuclei are significantly higher than the right and left crus I and vermis ROIs, whereas tCr is significantly lower compared to the right and left Crus I and vermis ROIs. Similarly, dentate nuclei has higher tCho, tNAA, and myo-ins levels compared to the vermis ROIs. Similar findings were also observed for water-scaled metabolite levels and metabolite ratios (Supporting Information Tables S2 and S3 for metabolite levels; Supporting Information Tables S5 and S6 for statistical findings). However, statistical significance degraded for water-scaled metabolite levels (Supporting Information Table S6).

## 4 | DISCUSSION

This study has demonstrated the advantage of rFOV (zoom) acquisition, zoomed, with a DW-CRT short TE semi-laser localization to improve the resolution and accuracy of whole cerebellum slice metabolic maps at 3T. The improved resolution and spectral quality-enabled reliable quantification of tNAA, tCr, tCho, Glx, and myo-ins from a nominal voxel volume of 62.5  $\mu\text{L}$ . The metabolite distribution maps for different ROIs in the cerebellum were consistent with the literature (see below). To our knowledge, this is the first study to have demonstrated a higher nominal resolution of 62.5  $\mu\text{L}$  at 3T for the cerebellum.

Implementing the rFOV acquisition at 3T for high-resolution MRSI faces several challenges caused by hardware and SNR ratio limitations. Mainly, high-resolution MRSI puts demands on maximum gradient amplitudes, rise time, and slew rate. To decrease the FOV while maintaining the acquisition matrix size, one might choose to increase the gradient amplitude and slew rate or to reduce the spectral bandwidth resulting in lower spectral sampling. In this study, to reach the nominal in-plane resolution of 2.5 mm  $\times$  2.5 mm, we decided to utilize reduced spectral bandwidth (625 Hz vs. 1250 Hz) compared to previous implementations.<sup>26</sup> The spectral bandwidth was doubled (1250 Hz) using an inverted readout gradient trajectory without causing any additional noise.<sup>24</sup> The use of DW-CRT and its reconstruction pipeline further contributed the SNR improvement, as discussed previously by Chiew et al.<sup>24</sup> Besides, a lower acquisition bandwidth of 40 kHz compared to the previous implementation of 80 kHz<sup>25,26,34</sup> minimized a larger amount of noise sampled due to the narrower frequency

range. Moreover, the 64-Channel head/neck coil allowed the incremental SNR gains in the peripheral ROIs closest to the coil elements such as the cerebellum.<sup>35</sup> Finally, additional SNR improvement was achieved through the use of metabolite cycling, allowing voxel-wise preprocessing steps.<sup>25</sup>

The present study did not directly compare this acquisition to others at 3T in which the nominal resolution ranged from 310  $\mu\text{L}$ <sup>18</sup> to 1210  $\mu\text{L}$ <sup>19</sup> for the cerebellum. We believe that our strategy offers substantial resolution improvement for 2D MRSI compared to the other implementations of the cerebrum at 3T and UHF. When the acquisition duration and magnetic field difference were considered, the achieved nominal resolution of 62.5  $\mu\text{L}$  and provided metabolite maps within 9 min 36 s in the cerebellum are comparable with the 3T and the UHF 2D MRSI in the cerebrum. For instance, a nominal voxel size of 24  $\mu\text{L}$  at 9.4T<sup>16</sup> and of 29  $\mu\text{L}$  at 7T<sup>36</sup> were achieved with acquisition durations of 46 and 42 min, respectively. With the use of constrained reconstruction methods, the proposed strategy is expected to provide higher resolution.<sup>15,37</sup>

The rFOV MRSI acquisition with a resolution of 62.5  $\mu\text{L}$  allowed reliable quantification of major brain metabolites in the cerebellum (Figures 2 and 3). Concentration distributions in the cerebellum of the reported metabolites revealed significant variations between the cerebellar vermis, white, and gray matter of both cerebellar hemispheres, and these were in line with previous MRSI and SV-MRS studies. For example, the high cerebellar total creatine level in the gray matter agreed with previous reports.<sup>19</sup> In addition, the higher Glx level obtained in cerebellar gray matter was consistent with the previous SV-MRS studies.<sup>38</sup> The highest total choline levels were observed in the cerebellar white matter, also in agreement with SV-MRS.<sup>38</sup>

The voxel-based comparisons of the SUIT atlas ROI<sup>4</sup> analyses of whole cerebellum slice metabolite maps demonstrated that metabolite distributions are spatially dependent. The dentate nuclei, the link in the cortico-cerebellar closed loop circuits,<sup>39</sup> had higher tNAA, tCho, and myo-ins levels. Because NAA was extensively distributed in the cerebellum and NAAG was very high in the deep cerebellar nuclei, higher tNAA levels observed in the dentate nuclei are in agreement with previous studies.<sup>40</sup> Because the dentate nuclei are embedded in the white matter having a higher glia-to-neuron ratio than gray matter,<sup>41</sup> myo-ins and tCho as markers of glial cells resulted in higher levels in the dentate nuclei. In line with the cyto and receptor architectonic mapping of glutamate receptors in the human cerebellum,<sup>42</sup> Glx levels were higher in the cerebellar cortex (right crus I, left crus I, and vermis) than in the dentate nuclei. Finally, higher creatine levels in the cerebellar cortex might suggest energy demand of Purkinje cells.<sup>19</sup> With the accurate coregistration between the MRSI and MNI template, high-quality group-average metabolite distributions of tNAA, tCr, tCho, Glx, and myo-ins were achieved.

The number of subjects is a limitation, and further experiments are required for the clinical validity of the proposed method. In addition, a single slice acquisition is not sufficient to map the entire cerebellum. Although the use of DW-CRT with  $\alpha = 1$  resulted in an improved SNR,<sup>24</sup> it deteriorates the point spread function and dilutes metabolite levels in small ROIs such as the dentate nuclei. Moreover, limited coverage of the single-slice



measurement of zoom MRSI can be overcome using multi-slice stacks with different slice orientations, providing improved coverage and resolution in the cerebellum.<sup>43</sup> The use of a long TR of 1.5 s and the cost of increased total acquisition duration due to the choice of adiabatic pulses can be mitigated by gradient-modulated offset-independent adiabaticity pulses.<sup>44</sup> Together with temporal interleaves ( $N_{ti} = 2$ ), total acquisition was 9 min 36 s. Recently, we have reduced acquisition duration to 4 min 48 s by reducing the spectral bandwidth to 893 Hz ( $N_{ti} = 1$ ) with the use of maximum slew rate of the gradient system (data were not shown). Although multiplet structures can still be resolved with acquisition window of 205 ms (corresponding to a spectral sampling resolution of 5 Hz), maintaining an high spectral sampling resolution is recommended for better separation.<sup>45</sup> As in all spectral subtraction-based techniques, the metabolite-cycling technique relies on homogenous  $B_1$  and  $B_0$  fields for an effective inversion profile. Although it had reported previously that the metabolite-cycling technique resulted in higher metabolite levels compared to the water suppression techniques,<sup>25,46</sup> the metabolite signals in the spectral range between 4.2 and 3.8 ppm might be affected by the adiabatic inversion pulses. Thus, further advances in hardware such as multi-transmit and shim coils are expected to improve the performance the metabolite cycling by providing homogeneous  $B_1$  and  $B_0$  fields in the cerebellum. Finally, the exact quantification of peaks might be affected by the use of simulated macromolecules and lipid removal procedures.

## 5 | CONCLUSION

In conclusion, the rFOV 2D MRSI resulted in very high-resolution metabolite maps of the cerebellum. These initial findings indicate that optimal methods can be developed for the future to generate a probabilistic metabolic atlas of the cerebellum.

## Supplementary Material

Refer to Web version on PubMed Central for supplementary material.

## Funding information

The study was supported by the Indiana CTSI and funded in part by grant #UL1TR001108 from the the National Institutes of Health (NIH), National Center for Advancing Translational Sciences (NCATS) Clinical and Translational Science Awards (CTSA)

## DATA AVAILABILITY STATEMENT

The data that support the findings of this study are available from the corresponding author upon reasonable request.

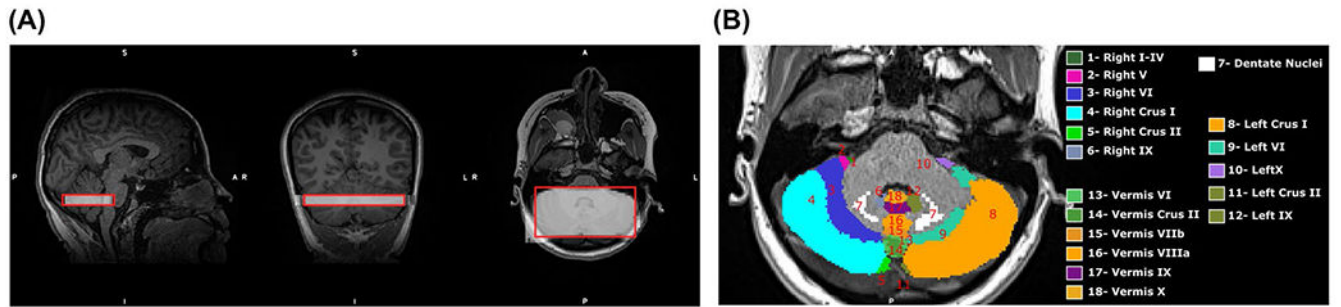
## REFERENCES

1. Van Essen DC, Donahue CJ, Glasser MF. Development and evolution of cerebral and cerebellar cortex. *Brain Behav Evol.* 2018;91:158–169. [PubMed: 30099464]
2. Howarth C, Gleeson P, Attwell D. Updated energy budgets for neural computation in the neocortex and cerebellum. *J Cereb Blood Flow Metab.* 2012;32:1222–1232. [PubMed: 22434069]
3. Diedrichsen J, Verstynen T, Schlerf J, Wiestler T. Advances in functional imaging of the human cerebellum. *Curr Opin Neurol.* 2010;23:382–387. [PubMed: 20581682]

4. Diedrichsen J, Balsters JH, Flavell J, Cussans E, Ramnani N. A probabilistic MR atlas of the human cerebellum. *Neuroimage*. 2009;46:39–46. [PubMed: 19457380]
5. King M, Hernandez-Castillo CR, Poldrack RA, Ivry RB, Diedrichsen J. Functional boundaries in the human cerebellum revealed by a multi-domain task battery. *Nat Neurosci*. 2019;22:1371–1378. [PubMed: 31285616]
6. Bürk K Ataxia scales for the clinical evaluation. In: Gruol DL, Koibuchi N, Manto M, Molinari M, Schmahmann JD, Shen Y, eds. *Essentials of Cerebellum and Cerebellar Disorders: A Primer For Graduate Students*. Cham, Switzerland: Springer International Publishing; 2016:513–520.
7. Fatemi SH. Cerebellar pathology in autism. In: Gruol DL, Koibuchi N, Manto M, Molinari M, Schmahmann JD, Shen Y, eds. *Essentials of Cerebellum and Cerebellar Disorders: A Primer For Graduate Students*. Cham, Switzerland: Springer International Publishing; 2016:539–543.
8. Kheradmand A, Kim JS, Zee D. Cerebellum and oculomotor deficits. In: Gruol DL, Koibuchi N, Manto M, Molinari M, Schmahmann JD, Shen Y, eds. *Essentials of Cerebellum and Cerebellar Disorders: A Primer For Graduate Students*. Cham, Switzerland: Springer International Publishing; 2016:471–475.
9. Schmahmann JD. The cerebellar cognitive affective syndrome and the neuropsychiatry of the cerebellum. In: Gruol DL, Koibuchi N, Manto M, Molinari M, Schmahmann JD, Shen Y, eds. *Essentials of Cerebellum and Cerebellar Disorders: A Primer For Graduate Students*. Cham, Switzerland: Springer International Publishing; 2016:499–511.
10. Öz G, Alger JR, Barker PB, et al. Clinical proton MR spectroscopy in central nervous system disorders. *Radiology*. 2014;270:658–679. [PubMed: 24568703]
11. Deelchand DK, Adanyeguh IM, Emir UE, et al. Two-site reproducibility of cerebellar and brainstem neurochemical profiles with short-echo, single-voxel MRS at 3T. *Magn Reson Med*. 2015;73:1718–1725. [PubMed: 24948590]
12. Long Z, Dyke JP, Ma R, Huang CC, Louis ED, Dydak U. Reproducibility and effect of tissue composition on cerebellar GABA MRS in an elderly population. *NMR Biomed*. 2015;28:1315–1323. [PubMed: 26314380]
13. Maudsley AA, Andronesi OC, Barker PB, et al. Advanced magnetic resonance spectroscopic neuroimaging: Experts' consensus recommendations. *NMR Biomed*. 2020;e4309. [PubMed: 32350978]
14. Moser P, Eckstein K, Hingerl L, et al. Intra-session and inter-subject variability of 3D-FID-MRSI using single-echo volumetric EPI navigators at 3T. *Magn Reson Med*. 2020;83:1920–1929. [PubMed: 31721294]
15. Lam F, Ma C, Clifford B, Johnson CL, Liang Z-P. High-resolution 1H-MRSI of the brain using SPICE: Data acquisition and image reconstruction. *Magn Reson Med*. 2016;76:1059–1070. [PubMed: 26509928]
16. Nassirpour S, Chang P, Henning A. High and ultra-high resolution metabolite mapping of the human brain using 1H FID MRSI at 9.4T. *Neuroimage*. 2018;168:211–221. [PubMed: 28025130]
17. Hingerl L, Strasser B, Moser P, et al. Clinical high-resolution 3D-MR spectroscopic imaging of the human brain at 7 T. *Invest Radiol*. 2020;55:239–248. [PubMed: 31855587]
18. Maudsley AA, Domenig C, Govind V, et al. Mapping of brain metabolite distributions by volumetric proton MR spectroscopic imaging (MRSI). *Magn Reson Med*. 2009;61:548–559. [PubMed: 19111009]
19. Jacobs MA, Horská A, van Zijl PC, Barker PB. Quantitative proton MR spectroscopic imaging of normal human cerebellum and brain stem. *Magn Reson Med*. 2001;46:699–705. [PubMed: 11590646]
20. Pfeuffer J, van de Moortele P-F, Yacoub E, et al. Zoomed functional imaging in the human brain at 7 Tesla with simultaneous high spatial and high temporal resolution. *Neuroimage*. 2002;17:272–286. [PubMed: 12482083]
21. Sun H, Fessler JA, Noll DC, Nielsen J-F. Rapid inner-volume imaging in the steady-state with 3D selective excitation and small-tip fast recovery (STFR) imaging. *Magn Reson Med*. 2016;76:1217–1223. [PubMed: 26507586]

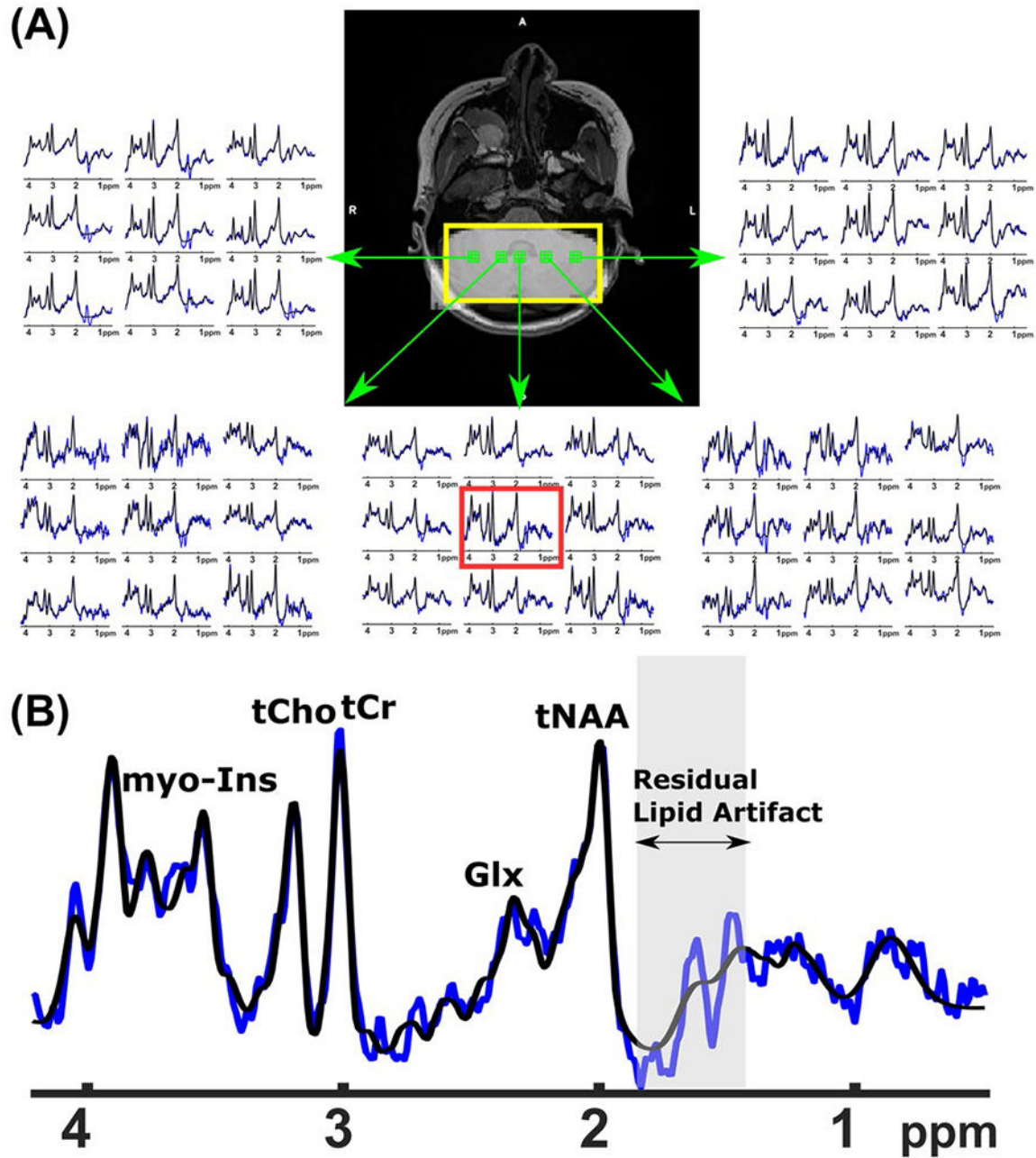
22. Golay X, Gillen J, van Zijl PCM, Barker PB. Scan time reduction in proton magnetic resonance spectroscopic imaging of the human brain. *Magn Reson Med*. 2002;47:384–387. [PubMed: 11810683]
23. Maudsley AA, Matson GB, Hugg JW, Weiner MW. Reduced phase encoding in spectroscopic imaging. *Magn Reson Med*. 1994;31:645–651. [PubMed: 8057817]
24. Chiew M, Jiang W, Burns B, et al. Density-weighted concentric rings k-space trajectory for 1H magnetic resonance spectroscopic imaging at 7 T. *NMR Biomed*. 2018;31:e3838.
25. Emir UE, Burns B, Chiew M, Jezzard P, Thomas MA. Non-water-suppressed short-echo-time magnetic resonance spectroscopic imaging using a concentric ring k-space trajectory. *NMR Biomed*. 2017;30:e3714.
26. Steel A, Chiew M, Jezzard P, et al. Metabolite-cycled density-weighted concentric rings k-space trajectory (DW-CRT) enables high-resolution 1 H magnetic resonance spectroscopic imaging at 3-Tesla. *Sci Rep*. 2018;8:7792. [PubMed: 29773892]
27. Fessler JA, Sutton BP. Nonuniform fast Fourier transforms using min-max interpolation. *IEEE Trans Signal Process*. 2003;51:560–574.
28. Cabanes E, Confort-Gouny S, Le Fur Y, Simond G, Cozzone PJ. Optimization of residual water signal removal by HLSVD on simulated short echo time proton MR spectra of the human brain. *J Magn Reson*. 2001;150:116–125. [PubMed: 11384169]
29. Bilgic B, Chatnuntaweck I, Fan AP, et al. Fast image reconstruction with L2-regularization. *J Magn Reson Imaging*. 2014;40:181–191. [PubMed: 24395184]
30. Provencher SW. Automatic quantitation of localized in vivo 1H spectra with LCModel. *NMR Biomed*. 2001;14:260–264. [PubMed: 11410943]
31. Quadrelli S, Mountford C, Ramadan S. Hitchhiker’s guide to voxel segmentation for partial volume correction of in vivo magnetic resonance spectroscopy. *Magn Reson Insights*. 2016;9:1–8. [PubMed: 27147822]
32. Jenkinson M, Beckmann CF, Behrens TEJ, Woolrich MW, Smith SM. FSL. *Neuroimage*. 2012;62:782–790. [PubMed: 21979382]
33. Benjamini Y, Hochberg Y. Controlling the false discovery rate: A practical and powerful approach to multiple testing. *J R Stat Soc Series B Stat Methodol*. 1995;57:289–300.
34. Alhulail AA, Patterson DA, Xia P, et al. Fat–water separation by fast metabolite cycling magnetic resonance spectroscopic imaging at 3 T: A method to generate separate quantitative distribution maps of musculoskeletal lipid components. *Magn Reson Med*. 2020;84:1126–1139. [PubMed: 32103549]
35. Keil B, Blau JN, Biber S, et al. A 64-channel 3T array coil for accelerated brain MRI. *Magn Reson Med*. 2013;70:248–258. [PubMed: 22851312]
36. Hangel G, Strasser B, Povazan M, et al. Ultra-high resolution brain metabolite mapping at 7 T by short-TR Hadamard-encoded FID-MRSI. *Neuroimage*. 2018;168:199–210. [PubMed: 27825954]
37. Klauser A, Courvoisier S, Kasten J, et al. Fast high-resolution brain metabolite mapping on a clinical 3T MRI by accelerated 1H-FID-MRSI and low-rank constrained reconstruction. *Magn Reson Med*. 2019;81:2841–2857. [PubMed: 30565314]
38. Emir UE, Auerbach EJ, Moortele P-FVD, et al. Regional neurochemical profiles in the human brain measured by 1H MRS at 7 T using local B1 shimming. *NMR Biomed*. 2012;25:152–160. [PubMed: 21766380]
39. Jaeger D, Lu H. Cerebellar nuclei. In: Gruol DL, Koibuchi N, Manto M, Molinari M, Schmähmann JD, Shen Y, eds. *Essentials of Cerebellum and Cerebellar Disorders: A Primer For Graduate Students*. Cham, Switzerland: Springer International Publishing; 2016:311–315.
40. Moffett JR, Namboodiri AMA. Expression of N-acetylaspartate and N-acetylaspartylglutamate in the nervous system. In: Moffett JR, Tieman SB, Weinberger DR, Coyle JT, Namboodiri AMA, eds. *N-Acetylaspartate. Advances in Experimental Medicine and Biology*. Boston, MA: Springer; 2006:7–26.
41. Azevedo FAC, Carvalho LRB, Grinberg LT, et al. Equal numbers of neuronal and nonneuronal cells make the human brain an isometrically scaled-up primate brain. *J Comp Neurol*. 2009;513:532–541. [PubMed: 19226510]

42. Palomero-Gallagher N, Chapter Zilles K. 24 - Cyto- and receptor architectonic mapping of the human brain. In: Huitinga I, Webster MJ, eds. *Handbook of Clinical Neurology: Brain Banking*. Vol. 150. Amsterdam, The Netherlands: Elsevier; 2018:355–387.
43. Shilling RZ, Robbie TQ, Bailloeuil T, Mewes K, Mersereau RM, Brummer ME. A super-resolution framework for 3-D high-resolution and high-contrast imaging using 2-D multislice MRI. *IEEE Trans Med Imaging*. 2009;28:633–644. [PubMed: 19272995]
44. Tannús A, Garwood M. Adiabatic pulses. *NMR Biomed*. 1997;10:423–434. [PubMed: 9542739]
45. Dydak U, Meier D, Lamerichs R, Boesiger P. Trading spectral separation at 3T for acquisition speed in multi spin-echo spectroscopic imaging. *AJNR Am J Neuroradiol*. 2006;27:1441–1446. [PubMed: 16908554]
46. Chang P, Nassirpour S, Avdievitch N, Henning A. Non-water-suppressed 1H FID-MRSI at 3T and 9.4T. *Magn Reson Med*. 2018;80:442–451. [PubMed: 29285781]



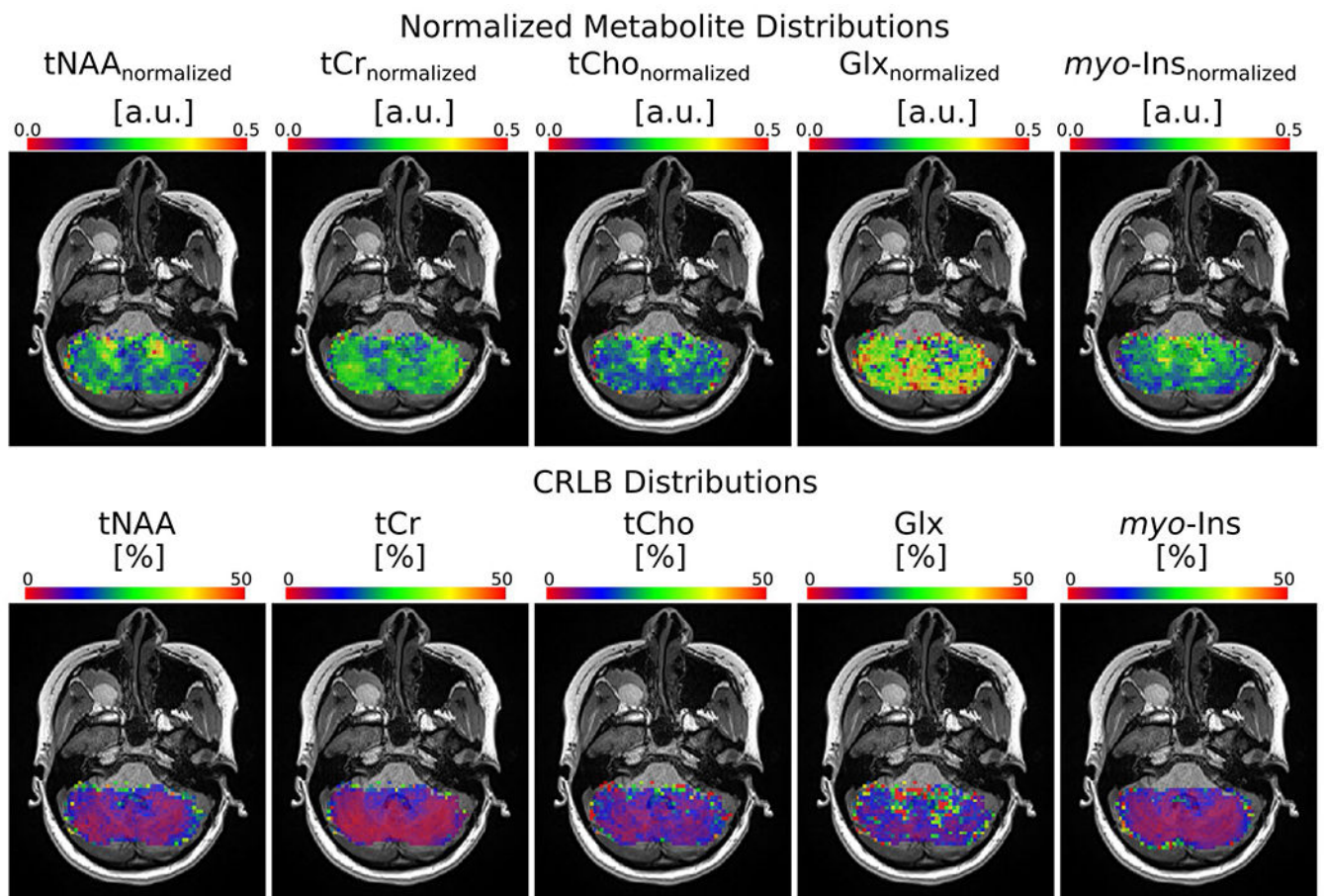
**FIGURE 1.**

(A) Representative semi-LASER localization (red boxes) and resulting water image of MRSI acquisition (gray shade) overlaid on top of high-resolution MPRAGE images. (B) ROI analysis is illustrated on the same subjects' MPRAGE axial image. Numbers from 1 to 18 represent ROIs in the cerebellar MNI FNIRT Maxprob thr25-2 mm SUI atlas. MRSI, MRS imaging; ROI, region of interest



**FIGURE 2.**

(A) Extracted spectra (blue) from 9 voxels ( $2.5 \text{ mm} \times 2.5 \text{ mm} \times 10 \text{ mm}$  each) of 5 different volumes of interests with LCMoDel fit (black). The semi-LASER localization (yellow box) and resulting water image of MRSI acquisition (gray shade) overlaid on top of high-resolution MP-RAGE image. (B) A single spectrum (red box in (A)) illustrates the quality of the achieved spectrum (blue) and LCMoDel fit (black). Gray box shows residual lipid artifact due to the L2 lipid removal procedure

**FIGURE 3.**

Metabolite and CRLB distribution maps after the Gaussian filter obtained with rFOV MRSI from a subject. Normalized metabolite level maps from a nominal voxel dimension of 62.5  $\mu\text{L}$  for tNAA, tCr, tCho, Glx, and myo-ins overlaid on an anatomical image. a.u., arbitrary units; CRLB, Cramer-Rao lower bound; Glx, glutamate + glutamine levels; myo-ins, myo-inositol; rFOV, reduced FOV; tCho, total Cho; tCr, total Cr; tNAA, total NAA

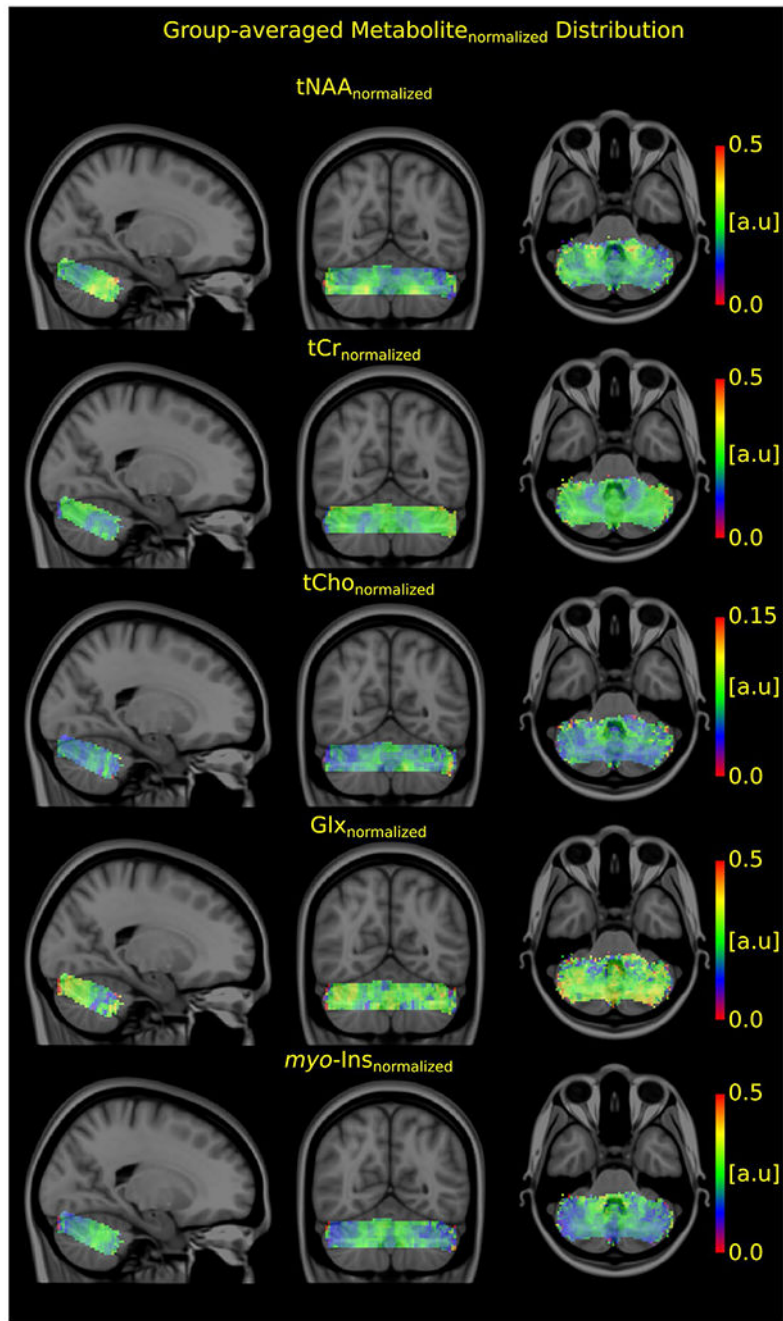


**FIGURE 4.** Group-average normalized metabolite maps overlaid on Montreal Neurological Institute-152 template



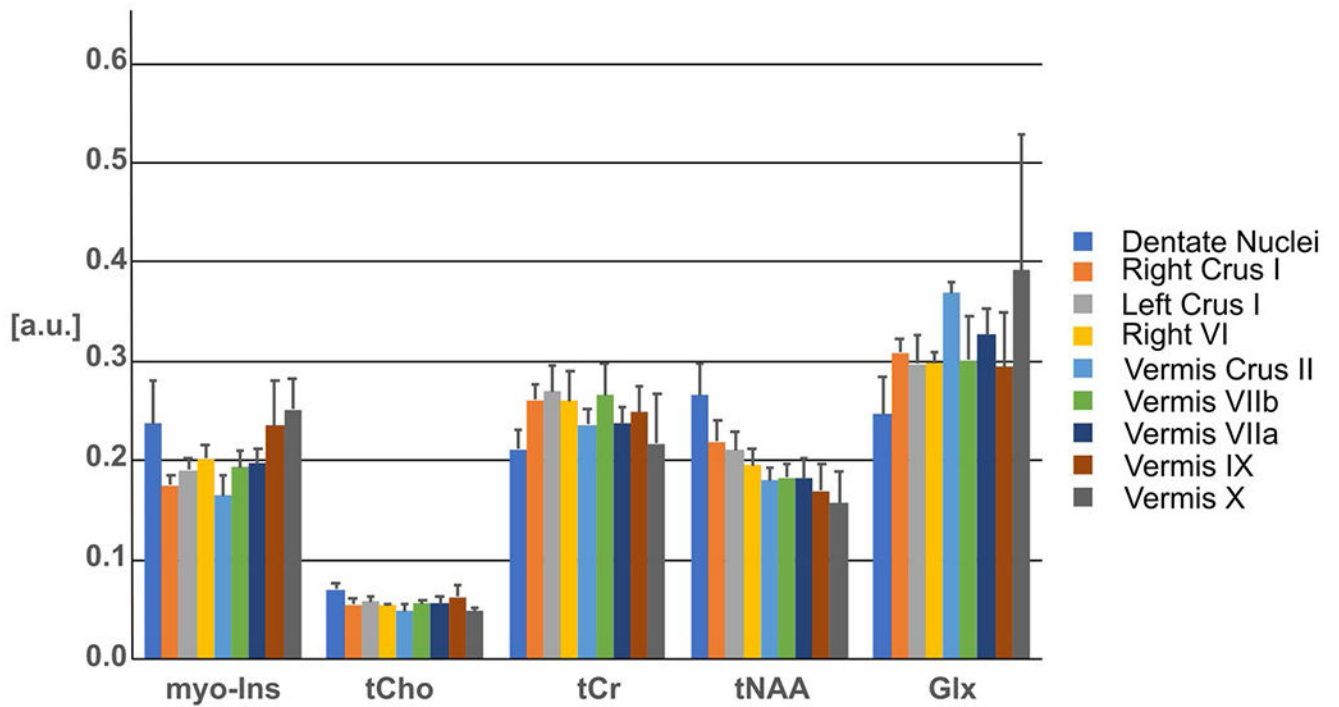


**FIGURE 5.**

Neurochemical profiles from different brain regions determined by LCMModel fitting of rFOV MRSI with a nominal resolution of  $2.5 \text{ mm} \times 2.5 \text{ mm} \times 10 \text{ mm}$  acquired at 3T. Only metabolites and ROIs that were quantified reliably are shown. Metabolites significantly different between regions ( $P < .05$ , ANOVA) were reported in the Supporting Information Table S4. Error bars: intersubject SD ( $N = 5$  for all brain regions). ANOVA, analysis of variance; T, Tesla

The list of ROIs and the mean number of voxels across subjects for each metabolite calculated in the center slice of semi-LASER VOI transformed to MP-RAGE dimensions

**TABLE 1**

| ROIs            | Mean Number of Voxel ± SD |           |           |           |           |  |
|-----------------|---------------------------|-----------|-----------|-----------|-----------|--|
|                 | tNAA                      | tCr       | tCho      | Glx       | Myo-ins   |  |
| Dentate nucleus | 150 ± 44                  | 150 ± 44  | 150 ± 44  | 131 ± 45  | 148 ± 41  |  |
| Right crus I    | 961 ± 89                  | 961 ± 89  | 926 ± 83  | 915 ± 109 | 945 ± 94  |  |
| Left crus I     | 817 ± 193                 | 817 ± 193 | 774 ± 191 | 761 ± 188 | 794 ± 198 |  |
| Right VI        | 488 ± 181                 | 488 ± 181 | 484 ± 179 | 471 ± 176 | 485 ± 183 |  |
| Vermis crus II  | 91 ± 27                   | 91 ± 27   | 91 ± 27   | 91 ± 27   | 91 ± 27   |  |
| Vermis VIIIB    | 45 ± 17                   | 45 ± 17   | 45 ± 17   | 45 ± 17   | 45 ± 17   |  |
| Vermis VIIIA    | 91 ± 7                    | 91 ± 7    | 91 ± 7    | 91 ± 7    | 91 ± 7    |  |
| Vermis IX       | 54 ± 20                   | 54 ± 20   | 54 ± 20   | 51 ± 21   | 54 ± 20   |  |
| Vermis X        | 38 ± 14                   | 38 ± 14   | 33 ± 16   | 35 ± 15   | 38 ± 15   |  |

Note: The resulted resolution of the center slice was  $0.9 \times 0.9 \text{ mm}^2$ . ROIs are in rows and metabolites are in columns.

Abbreviations: Glx, glutamate + glutamine levels; myo-ins, myo-inositol; ROI, region of interest; tCho, total Cho; tCr, total Cr; tNAA, total NAA; VOI, volume of interest.

TABLE 2

The list of ROIs and the mean CRLBs across subjects for each metabolite

| ROIs            | Mean CRLB $\pm$ SDs |                  |                 |                |                 |  |
|-----------------|---------------------|------------------|-----------------|----------------|-----------------|--|
|                 | tNAA                | tCr              | tCho            | Glx            | Myo-ins         |  |
| Dentate nucleus | 9.0 $\pm$ 1.9       | 8.3 $\pm$ 2.4    | 10.3 $\pm$ 2.0  | 26.3 $\pm$ 8.5 | 10.0 $\pm$ 3.7  |  |
| Right crus I    | 9.7 $\pm$ 1.9       | 6.4 $\pm$ 0.9    | 11.9 $\pm$ 1.7  | 15.1 $\pm$ 1.7 | 10.8 $\pm$ 1.6  |  |
| Left crus I     | 11.4 $\pm$ 1.6      | 6.7 $\pm$ 1.0    | 13.0 $\pm$ 2.5  | 17.4 $\pm$ 3.8 | 11.3 $\pm$ 2.2  |  |
| Right VI        | 7.2 $\pm$ 0.8       | 4.7 $\pm$ 1.1    | 8.7 $\pm$ 0.7   | 12.6 $\pm$ 0.9 | 6.7 $\pm$ 0.3   |  |
| Vermis crus II  | 6.5 $\pm$ 0.3       | 3.9 $\pm$ 0.4    | 8.4 $\pm$ 1.2   | 9.0 $\pm$ 1.2  | 6.9 $\pm$ 1.3   |  |
| Vermis. VIIIB   | 6.2 $\pm$ 1.2       | 3.5 $\pm$ 0.5    | 7.2 $\pm$ 1.2   | 11.7 $\pm$ 3.1 | 5.8 $\pm$ 0.8   |  |
| Vermis VIIIA    | 7.2 $\pm$ 2.2       | 4.5 $\pm$ 0.9    | 8.3 $\pm$ 1.2   | 12.6 $\pm$ 4.5 | 6.6 $\pm$ 1.2   |  |
| Vermis IX       | 11.7 $\pm$ 5.0      | 6.2 $\pm$ 1.4    | 10.7 $\pm$ 1.9  | 18.3 $\pm$ 7.6 | 8.3 $\pm$ 1.3   |  |
| Vermis X        | 22.4 $\pm$ 7.0      | 16.25 $\pm$ 11.0 | 29.0 $\pm$ 12.2 | 22.4 $\pm$ 9.7 | 17.0 $\pm$ 11.2 |  |

Note: ROIs are in rows, and metabolites are in columns.

Abbreviations: CRLB, Cramer-Rao lower bound.